


 Cite this: *RSC Adv.*, 2022, 12, 16723

# Preparation of a bionic lotus leaf microstructured surface and its drag reduction performance

 Huan Wang,<sup>ID</sup><sup>ab</sup> Guihang Luo,<sup>a</sup> Lei Chen,<sup>a</sup> Yuqiu Song,<sup>a</sup> Cuihong Liu<sup>a</sup>  
 and Liyan Wu<sup>ID</sup><sup>\*a</sup>

Reducing machinery surface friction resistance can improve the efficiency of energy utilization. The lotus leaf, as everyone knows, has a strong capacity for self-cleaning and hydrophobicity. In this paper, the bionic surface of the lotus leaf was prepared in large-area, and its drag reduction performance was studied by both numerical simulation and experimental analysis. Experimental results showed that the maximum drag reduction rate of the bionic surface was 6.29% which appeared at a velocity of 3 m s<sup>-1</sup>. The contact state between liquid and bionic surface changed from Cassie state to Wenzel state with the increase of water flow velocity. The surface free energies of the bionic surface and smooth surface were 1.09 mJ m<sup>-2</sup> and 14.26 mJ m<sup>-2</sup>, respectively. In the droplet rolling experiment, the water droplet was a hemisphere when it rolled on the smooth surface, while it was an ellipsoid on the bionic surface. This study provides a theoretical basis for the structural design of bionic drag reduction surfaces, which are expected to be applied in underwater vehicles.

Received 7th March 2022

Accepted 28th May 2022

DOI: 10.1039/d2ra01495e

[rsc.li/rsc-advances](https://rsc.li/rsc-advances)

## 1. Introduction

It is well known that the self-cleaning capacity and hydrophobicity of lotus leaves are related to the wax coat and papillae structure. The micro/nano hierarchy morphology of papillae can impact the surface energy of lotus leaves.<sup>1,2</sup> In previous reports, the interface with low surface energy has superior performance in antifouling,<sup>3</sup> anti-icing,<sup>4</sup> antifogging,<sup>5</sup> antireflection,<sup>6</sup> oil-water separation,<sup>7</sup> and so on. These extraordinary properties have stimulated the interest of researchers. How to prepare a superior performance bionic lotus leaf surface has been a research topic for years.<sup>8</sup> By the chemical vapor deposition method, Wang *et al.* prepared a lotus-leaf-like superhydrophobic carbon nanotube film with micro/nanoscale hierarchical structure, which could effectively prevent the small water droplets from penetrating the film.<sup>9</sup> By the nanosecond laser processing method, Hauschwitz *et al.* prepared lotus leaf double-scale structures on an aluminium alloy.<sup>10</sup> By the multi-scale stereolithography method, Li *et al.* prepared artificial lotus leaves with micropillar structure.<sup>11</sup> Das *et al.* prepared microstructures of lotus leaves by direct replication. However, the disadvantage of this method was that it was difficult to demould, and the size of the sample was limited by the size of the lotus leaf.<sup>12</sup> Bhushan *et al.* prepared a lotus-leaf-like surface by replicating micro patterns on silicon surfaces, and the

nanostructures were created by self-assembly of wax platelets (*n*-hexadecane) and tubules (*T. majus* and lotus).<sup>13</sup> Rong *et al.* prepared micro/nanostructures of lotus leaves on metal substrates by using a laser ablation method.<sup>14</sup>

Reducing energy consumption has attracted widespread attention. The drag reduction function of the superhydrophobic surface has increasingly attracted the interest of scholars and become a popular topic. The lotus-leaf-like superhydrophobic surface showed good drag reduction performance in previous studies.<sup>15,16</sup> Rong *et al.* analyzed the drag reduction performance of bionic lotus leaf surface by both numerical simulation and experiment analysis, and the maximum drag reduction rate reached 52.76% at velocity of 1.55 m s<sup>-1</sup>.<sup>14</sup> Sheng *et al.* studied the sustainability of the air layer on the lotus leaf surface and believed that the superhydrophobic surface can maintain a stable layer of air.<sup>17</sup> Lyu *et al.* showed that drag reduction of the superhydrophobic surface was mainly caused by the velocity slip of the fluid on solid-liquid interfaces.<sup>18</sup> Lu *et al.* explored the drag reduction mechanism of the bionic lotus leaf surface through the volume of the fluid simulation way, and the microstructure size with the optimal lubrication was obtained.<sup>19</sup>

From all the studies above, several relevant issues remain unresolved. For example, the contact states between water flow and hydrophobic surface at different speeds have not been explored. The area of the prepared bionic surface is too small to be applied in engineering, and the processing techniques are complicated. In this work, the drag reduction mechanism of the hydrophobic surface was studied by combining numerical simulation with actual experiment. The contact states between water flow and the hydrophobic surface under different speeds

<sup>a</sup>College of Engineering, Shenyang Agricultural University, Shenyang, 110866, P. R. China. E-mail: wly78528@syau.edu.cn

<sup>b</sup>Key Laboratory of Bionic Engineering, Ministry of Education, Jilin University, Changchun, 130022, P. R. China



were explored, and the relationship between drag reduction rate and water flow velocity was established by numerical analysis. The bionic surface was prepared by imitating the lotus leaf surface microstructure. The wettability and drag reduction performance of the bionic surface were analyzed, and the shape of the rolling water droplet was observed through the inclining bench experiment. The prepared bionic surface is expected to be utilized for the surface of underwater vehicle. This study provides a theoretical basis for the drag reduction research of hydrophobic surface.

## 2. Experiments

### 2.1 Materials

Lotus leaf was collected from Nanhu Lake, Changchun, China. Polydimethylsiloxane (PDMS) was obtained from Wuxi Fittes International Trade Limited Co., Ltd. PDMS is a kind of non-toxic, anti-wear, hydrophobic, and low surface energy polymer materials, which is widely used in cosmetics, brighteners, lubricants, release agents, water proof agent, *etc.*<sup>20–22</sup> The silicon wafer and mask plate were purchased from Suzhou Institute of Nano-Tech and Nano-Bionics, Chinese Academy of Sciences.

### 2.2 Microstructure of lotus leaves surface

Fig. 1(a) shows lotus leaves in the pond. The microstructure of lotus leaf surface was observed by scanning electron microscope (SEM), as shown in Fig. 1(b) and (c). There are many papilla microstructures on the surface of lotus leaf, as shown in Fig. 1(b), and the papilla structure resembles cylinder. Fig. 1(c) shows the magnified papilla structures. The diameter of papillae ranges from 2  $\mu\text{m}$  to 8  $\mu\text{m}$ , and the height ranges from 6  $\mu\text{m}$  to 12  $\mu\text{m}$ .

### 2.3 Establish of the simulation model

The simulation model was established for analysis of resistance and drag reduction mechanism, as shown in Fig. 2(a). In order to make it easier to build the 3D models and improve computing speed, the papillae structure on the surface of lotus leaf is regarded as cylinders structure in the numerical simulation, as shown in Fig. 2(b) and (c). The diameter of the cylinder is 5  $\mu\text{m}$ , the spacing between two adjacent cylinders is 10  $\mu\text{m}$ , and the height is 10  $\mu\text{m}$ . The diameter of the flow field is

0.5 mm and the length is 1 mm. The height of the sample is 24  $\mu\text{m}$ , the length is 148  $\mu\text{m}$ , and the width is 150  $\mu\text{m}$ .

In order to avoid the influence of the inlet effect on the flow field (Fig. 2(a)), the distance between the sample and the inlet is set as 0.5 mm. The fluid medium is water. The density is 998.2  $\text{kg m}^{-3}$ , and the dynamic viscosity coefficient is  $1.0 \times 10^{-3}$  Pa s. The hydraulic diameter of the model is 0.5 mm, and the wall is set as a non-slip wall. Turbulent dissipation will occur when the fluid flows through the sample surface. Therefore, the  $k$ - $\varepsilon$  equation was selected in this simulation.<sup>23</sup> The turbulent kinetic energy and turbulent intensity of the sample were calculated according to eqn (1)–(3).

$$I = 0.16(\text{Re})^{-1/8} \quad (\text{Re} = \rho u L / \mu) \quad (1)$$

$$k = \frac{3}{2}(uI)^2 \quad (2)$$

$$\varepsilon = C_\mu^{3/4} \frac{k^{3/2}}{l} \quad (l = 0.07L) \quad (3)$$

where  $I$  represents the turbulence intensity.  $\text{Re}$  is the Reynolds number,  $\rho$  the fluid density.  $u$  is the mean velocity of fluid.  $k$  is the turbulence kinetic energy and  $\mu$  is the viscosity coefficient.  $L$  is the characteristic length.  $C_\mu = 0.09$ .

### 2.4 Fabrication of imitating lotus leaf surface

The bionic samples were fabricated by the combination method of photolithography and vacuum casting. The sample preparation steps are as follows (Fig. 3).

(a) Cleaning and preheating: to clean contaminants on the surface of the silicon substrate, the substrate was washed in deionized water for 1 to 2 minutes. Then, it was heated in a vacuum drying oven for 2 to 3 minutes.

(b) Spin-on PR coating: dropping the photoresist on the silicon substrate. The rotation speed was gradually increased from 500 rpm to 3000 rpm.

(c) Soft heating and wafer edge exposure: the silicon substrate coated with photoresist was heated in a vacuum drying oven for 30–60 seconds at 95  $^\circ\text{C}$ , and the pressure was controlled between 0.1–0.3 MPa.

(d) Proximity printing: the distance between mask and photoresist was maintained in the range of 10–50  $\mu\text{m}$ .

(e) Post exposure heating: adjusting the temperature of the vacuum drying oven to 110–130  $^\circ\text{C}$  and keep it for 5 minutes.

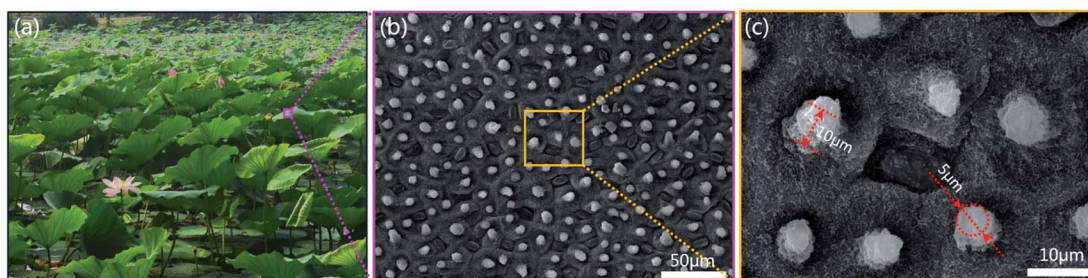


Fig. 1 The structure of lotus leaf. (a) Lotus leaves in the pond. (b) SEM image of the lotus leaf. (c) Magnified papilla microstructures.



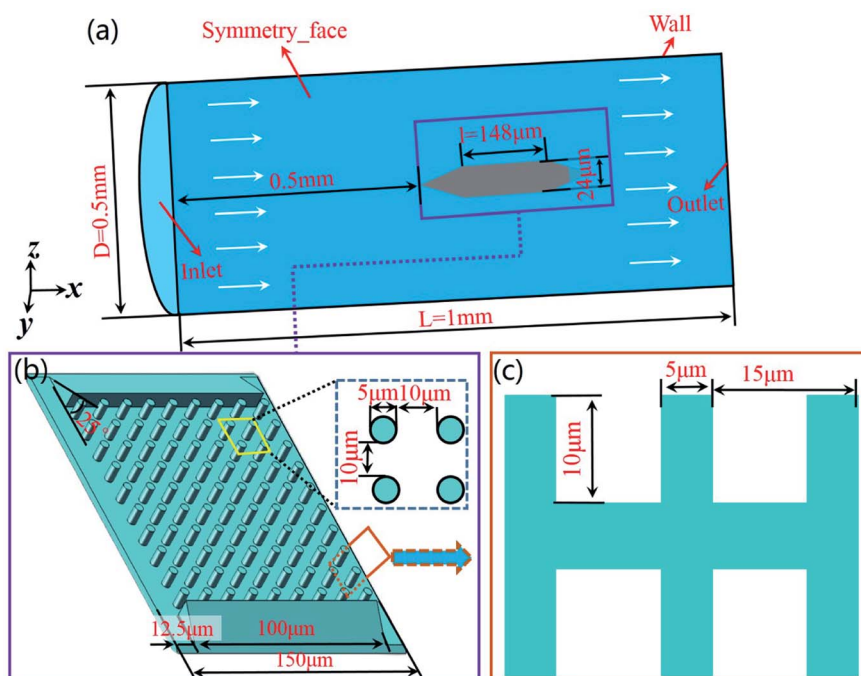


Fig. 2 Establishment of simulation model. (a) The flow field model for numerical simulation. (b) The sample structure for numerical simulation. (c) The size of microstructure.

(f) Development: the silicon substrate was coated again with (tetramethylammonium hydroxide) on the layer of photoresist.

(g) Hardening and sculpture: to completely remove the solvent in the photoresist and obtain the negative template of papilla microstructure.

(h) Coating: spraying a layer of release agent on the negative template. Mixing Sylguard-184A and Sylguard-184B in a ratio of 10 to 1. Then, dropping 20 mL of the mixture on the surface of negative template.

(i) Heat curing: placing the negative template in a vacuum drying oven for 1 hour. The pressure was maintained at 0.2–0.4 MPa and the temperature was maintained at 70 °C.

(j) Finally, the template was demoulded, the bionic surface with papillae microstructure was obtained.

## 2.5 Experiment of the inclining bench

When a droplet moves on a inclining bench, the movement of the center of gravity of the droplet can be used to analyze the effect of drag reduction.<sup>24</sup> In this study, the inclining bench experiment was carried out at 25 °C, and the angle of the inclining bench was 40°, as shown in Fig. 4(a). The smooth surface and bionic surface were pasted onto the inclining bench, as shown in Fig. 4(b). The water droplet volume is 0.01

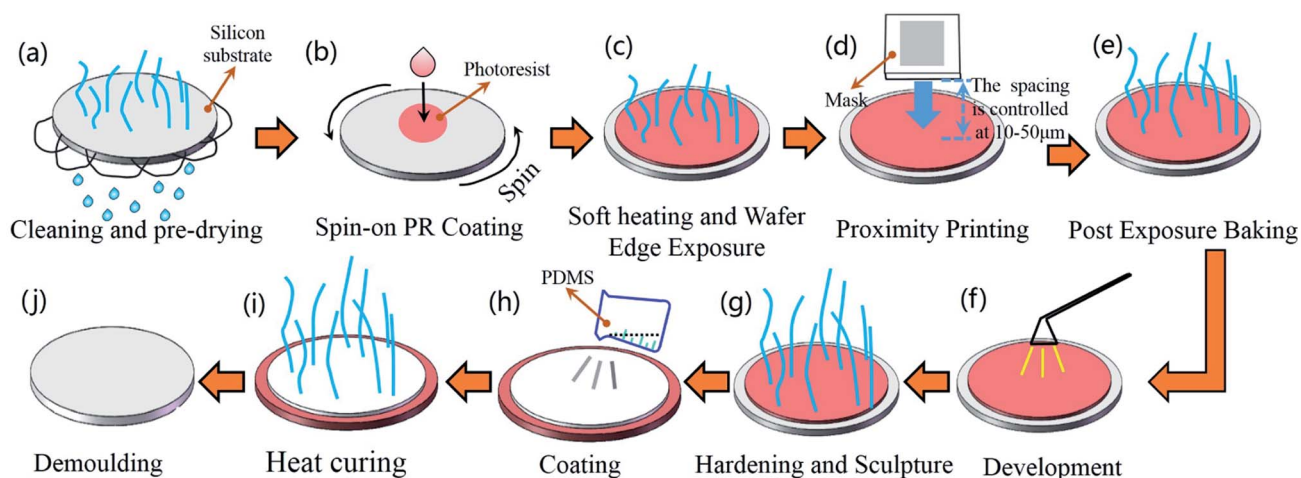


Fig. 3 Fabrication process of bionic surface.



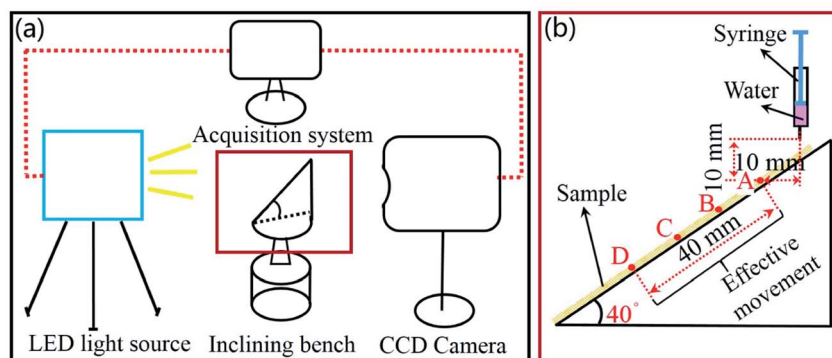


Fig. 4 Droplet rolling experiment. (a) Schematic diagram of the experimental device. (b) Inclining bench.

mL. Both the horizontal and vertical distances of the syringe from point A are 10 mm.

## 2.6 The tunnel experiment

The drag reduction effect of the bionic surface was tested through the water tunnel experiment. Fig. 5 shows the schematic diagram of the experimental device. The velocity of water flowing was controlled by the valve, and the resistance of the sample was calculated by comparing the pressure before and after the sample.

# 3. Results and discussion

## 3.1 Properties of the bionic sample

The size of the bionic sample is 50 mm × 50 mm. The morphology and elements of the bionic surface were analyzed by SEM and Energy Dispersive Spectroscopy (EDS). From the Fig. 6(a) and (b), the bionic surface is precisely prepared by the combination method of photolithography and vacuum casting. Fig. 6(c) shows the cross-sectional view of the bionic surface. Fig. 6(d) shows the major elements of the bionic surface, which mainly consists of C, Si and O elements. The atomic percentage of C, Si and O are 44.3%, 29.7% and 26.0%, respectively.

Fig. 7 shows the phase analysis of X-ray diffraction (XRD) and Raman spectra of the bionic surface. The X-ray diffraction of the

bionic surface reaches its peak value at 24.5°, as shown in Fig. 7(a). According to Joint Committee on Powder Diffraction Standards (JCPDS), this peak value matches the PDMS diffraction peak. The peak values appear at 2905 cm<sup>-1</sup> and 2960 cm<sup>-1</sup>, which are associated with the symmetric and anti-symmetric stretching vibration of -CH<sub>3</sub>, as exhibited in Fig. 7(b). The peak value at 495 cm<sup>-1</sup> corresponds to the Si-O-Si symmetric stretching.<sup>25</sup>

## 3.2 Numerical simulation results

In the flow rate range of from 1 to 9 m s<sup>-1</sup>, the pressure drag, viscous drag and total drag were figured out by numerical simulation, as exhibited in Table 1. It can be concluded that the drag force gradually increases with the increase of fluid velocity. According to eqn (4),<sup>26</sup> the drag reduction rate of the bionic surface can be calculated.

$$\eta = \left( \frac{F_{ts} - F_{tb}}{F_{ts}} \right) \times 100\% \quad (4)$$

where  $\eta$  is drag reduction rate,  $F_{ts}$  is the resistance of the smooth surface,  $F_{tb}$  is the resistance of the bionic surface.

As shown in Fig. 8(a), the drag reduction rate of the bionic surface gradually increases with the increase of velocity from 1.0 m s<sup>-1</sup> to 3.0 m s<sup>-1</sup>, and the maximum drag reduction rate is 6.29% when velocity is 3.0 m s<sup>-1</sup>. However, the drag reduction

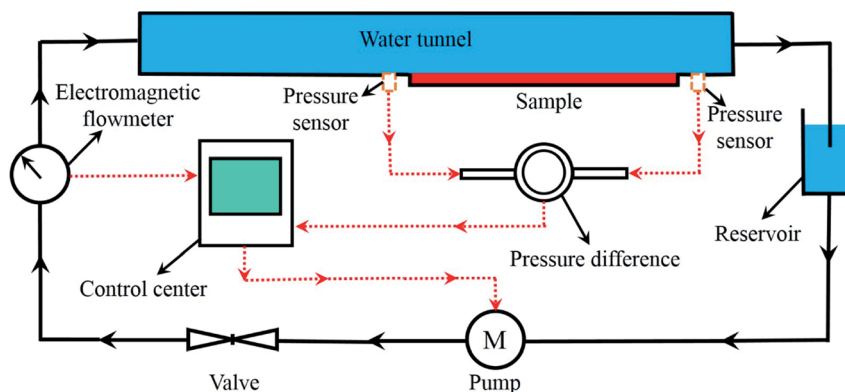


Fig. 5 Schematic diagram of the water tunnel experiment device.



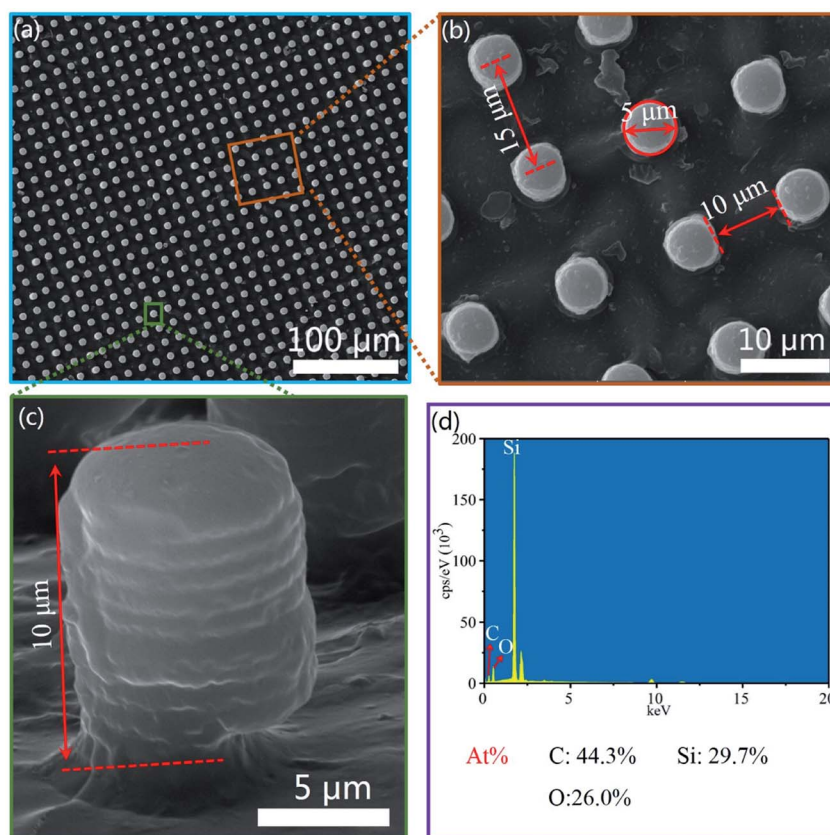


Fig. 6 The morphologies and elements distribution on the bionic sample surface. (a and b) The micro morphologies of the bionic surface at 1000 and 5000 times magnification. (c) The cross section structure of the bionic surface. (d) The elements distribution of ESD results.

rate rapidly declines with the increase of water flow velocity from the velocity of  $3.0 \text{ m s}^{-1}$  to  $9.0 \text{ m s}^{-1}$ , and the bionic surface will lose the drag reduction function after  $9.0 \text{ m s}^{-1}$ . Fig. 8(b) shows the near-wall flow velocity of the bionic surface and smooth surface, and the velocity gradient  $\Delta V_b$  is less than  $\Delta V_s$  ( $\Delta V_b$  is the velocity gradient of bionic surface, and  $\Delta V_s$  is the velocity gradient of the smooth surface). When the inlet water flow velocity is  $1 \text{ m s}^{-1}$ , the water flow velocity of the bionic surface is  $0.18 \text{ m s}^{-1}$ . The velocity slip appears on the bionic

surface, and the slip length is  $10 \mu\text{m}$ . On the contrary, there is no velocity slip on the smooth surface, and the water flow velocity of the smooth surface is  $0 \text{ m s}^{-1}$ . Therefore, the existence of microstructure dramatically reduce the thickness of the viscous sublayer and transition layer. The velocity on the bionic surface quickly increases and finally reaches the velocity of the center zone. Hence, the shear stress of the bionic surface is lower than that of a smooth surface, according to eqn (5).<sup>27</sup>

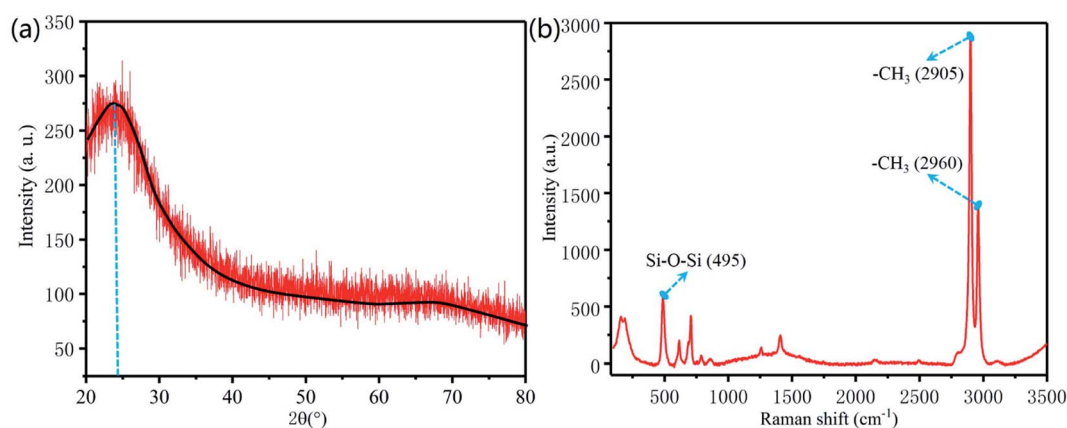


Fig. 7 Component analysis of the bionic surface. (a) X-ray analysis (b) Raman analysis.

Table 1 Comparison between the resistance of the smooth surface and bionic surfaces

Velocity (m s <sup>-1</sup> )		1	3	5	7	9
Smooth surface	Pressure drag ( <i>N</i> )	$6.8164 \times 10^{-7}$	$4.4220 \times 10^{-6}$	$1.1045 \times 10^{-5}$	$2.0320 \times 10^{-5}$	$3.2089 \times 10^{-5}$
	Viscous drag ( <i>N</i> )	$3.2640 \times 10^{-6}$	$1.5032 \times 10^{-5}$	$3.1868 \times 10^{-5}$	$5.2718 \times 10^{-5}$	$7.7002 \times 10^{-5}$
	Total drag ( <i>N</i> )	$3.9456 \times 10^{-6}$	$1.9454 \times 10^{-5}$	$4.2913 \times 10^{-5}$	$7.3037 \times 10^{-5}$	$1.0909 \times 10^{-4}$
Bionic surface	Pressure drag ( <i>N</i> )	$1.3833 \times 10^{-6}$	$8.2530 \times 10^{-6}$	$2.0735 \times 10^{-5}$	$3.9124 \times 10^{-5}$	$6.3666 \times 10^{-5}$
	Viscous drag ( <i>N</i> )	$2.3579 \times 10^{-6}$	$9.9765 \times 10^{-6}$	$2.0001 \times 10^{-5}$	$3.1946 \times 10^{-5}$	$4.5565 \times 10^{-5}$
	Total drag ( <i>N</i> )	$3.7412 \times 10^{-6}$	$1.8230 \times 10^{-5}$	$4.0737 \times 10^{-5}$	$7.1070 \times 10^{-5}$	$1.0923 \times 10^{-4}$
Drag reduction rate (%)	5.18	6.29	5.07	2.69	-0.13	

$$\tau = \mu \frac{d\mu}{dy} \quad (5)$$

where  $\tau$  is shear stress,  $\mu$  is the dynamic viscosity of the fluid and  $\frac{d\mu}{dy}$  is the velocity gradient.

When the water flow velocity on the bionic surface is lower than  $3 \text{ m s}^{-1}$ , the state between the bionic surface and the water flow is Cassie state.<sup>28</sup> Due to the effect of surface tension, the water flow cannot easily immerse into the gaps between papillae, and the air is trapped in the gaps, as illustrated in Fig. 9(a). The angle  $\theta$  between air and water will gradually decrease with the increase of flow rate, and the drag reduction rate also increases. When the water pressure is equal to the surface tension, the angle between the air and the liquid is  $\theta = 0$ , as revealed in Fig. 9(b). When the drag reduction rate reaches the maximum, the length of the velocity slip also reaches the maximum. The liquid will gradually immerse into the gaps between papillae as the flow velocity continues to increase. The contact state between the bionic surface and the fluid changes to the Wenzel–Cassie state, as shown in Fig. 9(c). As the flow velocity continues to increase, the angle between air and liquid increases, and the drag reduction rate decreases gradually. The fluid fully enters into the gaps between papillae, as shown in Fig. 9(d). The contact state between the fluid and bionic surface changes to the Wenzel state, and the velocity slip on the bionic surface will disappear. Under Wenzel state, the existence of

microstructure hinders the water flowing, therefore the drag reduction effect of bionic surface disappears.

### 3.3 Experiment results

By using the water tunnel, the drag reduction effect of the bionic surface was measured. Results show that the maximum drag reduction rate of the bionic surface is 7.26% at velocity of  $3.0 \text{ m s}^{-1}$ , which is a little different from the numerical simulation result. There are several reasons. First, the grid density in the numerical simulation can affect the accuracy of numerical analysis results. Second, in the actual water tunnel experiment, there are inevitably some tiny bubbles in the water flow. Even if the bubble removal treatment is carried out before the experiment, there is still difference from the pure water medium used in the simulation analysis. Last, the accuracies of valves and sensors in the experimental device also may affect the results. In summary, these factors lead to the difference between the numerical analysis and the experimental results. However, both numerical simulation and experiment results show the same trend of drag reduction.

In the previous studies,<sup>29</sup> the result shows that the contact angle between water droplets and PDMS surface decreases gradually with the increase of temperature. When the temperature is between  $0^\circ\text{C}$  and  $40^\circ\text{C}$ , the contact angle is about  $153^\circ$ , which almost remains same. When the temperature is between  $40^\circ\text{C}$  and  $60^\circ\text{C}$ , the contact angle decreases gradually to  $110^\circ$ . In this study, the experiments were carried out at  $25^\circ\text{C}$ , and the

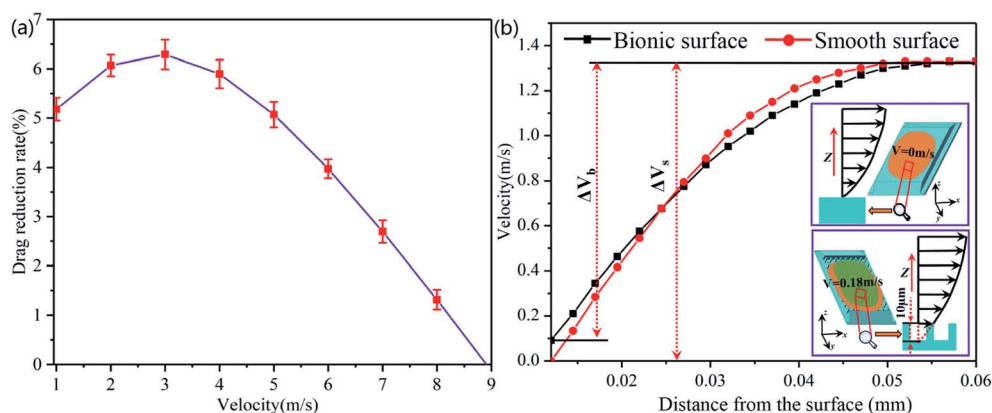


Fig. 8 The result of numerical analysis. (a) Drag reduction rate of the bionic surface. (b) The velocity gradient of bionic surface and smooth surface.



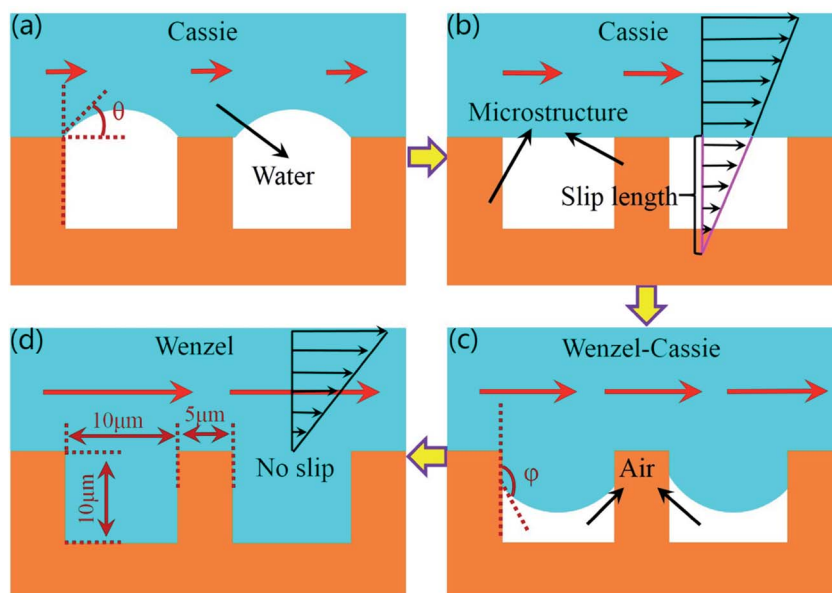


Fig. 9 The contact state between liquid and wall. (a) Depinned-out state. (b) Pinned state. (c) Pinned-in state. (d) Fully wetted state.

static contact angles of water droplets on bionic surface and smooth surface were measured through the contact angle instrument (DSA-25A). The static contact angle of water droplet on smooth surface is  $120.4^\circ$ , as shown in Fig. 10(a), and  $156.6^\circ$  on the bionic surface, as shown in Fig. 10(b). According to eqn (6),<sup>30</sup> the surface free energy ( $\gamma_s$ ) of smooth surface and bionic surfaces are  $14.26 \text{ mJ m}^{-2}$  and  $1.09 \text{ mJ m}^{-2}$ , respectively. Therefore, it can be concluded that the bionic microstructure

can reduce the surface free energy and improve surface hydrophobicity.

$$\cos \theta = -1 + 2\sqrt{\frac{\gamma_s}{\gamma_L}} \left[ 1 - \beta(\gamma_s - \lambda_L)^2 \right] \quad (6)$$

where  $\theta$  is the contact angle,  $\gamma_s$  is the surface free energy of a smooth surface or bionic surface.  $\beta$  is a constant with a value of  $1.1229 \times 10^{-4} (\text{m}^2 \text{mJ}^{-1})^2$  and the surface energy of water ( $\gamma_L$ ) is  $72.8 \text{ mJ m}^{-2}$ .

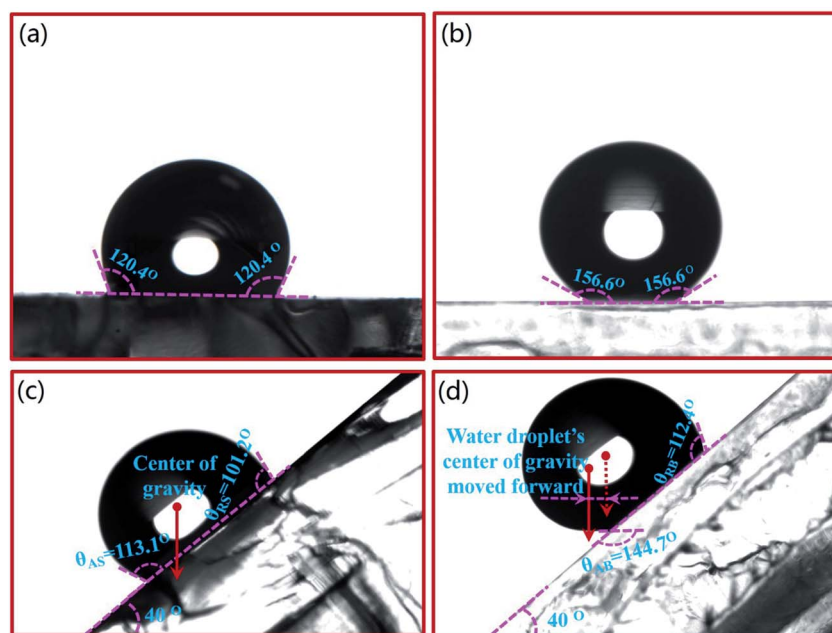


Fig. 10 The wettability of smooth surface and bionic surface. (a) Static contact angle of smooth surface (b) Static contact angle of bionic surface (c) Rolling state of droplet on a smooth surface (d) Rolling state of droplet on the bionic surface.



The angle of the inclining bench is gradually increased from  $0^\circ$  to  $25^\circ$ . When the angle is  $25^\circ$ , the water droplet begins to roll down. The rolling angle  $25^\circ$  seems large for superhydrophobicity surface. The rolling angle is related to the chemical composition and the microstructure of the surface.<sup>31</sup> If accurate nanostructures are achieved on the bionic surface, the rolling angle would be further reduced. Here, the water droplets rolling state was analyzed when the bench was remained at  $40^\circ$ . Fig. 10(c) and (d) shows the shape of the droplet rolling to point D. The shape of water droplet on a smooth surface is hemispherical, as shown in Fig. 10(c). The advancing contact angle ( $\theta_{AS}$ ) and receding contact angle ( $\theta_{RS}$ ) of water droplet is  $113.1^\circ$  and  $101.2^\circ$ , respectively. Conversely, the shape of the droplet rolling on the bionic surface is ellipsoidal, and the center of gravity moves forward (Fig. 10(d)). The advancing contact angle ( $\theta_{AB}$ ) and receding contact angle ( $\theta_{RB}$ ) of the water droplet is  $144.7^\circ$  and  $112.4^\circ$ , respectively, as shown in Fig. 10(d). It is found that the advancing contact angle and receding contact angle of the water droplet are significantly lower than the static contact angle on the bionic surface. The rolling speed of the water droplet increases and immerses into the papillae gaps gradually. The surface free energy of smooth surface is  $13.17 \text{ mJ m}^{-2}$  higher than that of bionic surface. However, the surface free energy of the bionic surface and adhesion of water droplet is lower, and the rolling speed of the water droplet is faster. The existence of microstructure reduces the contact area between the droplets and the surface. Due to the surface tension, the water droplet cannot completely immerse into the papillae gaps when it rolls from point A to point D. The contact state between water droplet and the bionic surface is Cassie or Wenzel–Cassie state, and air is trapped in the papillae gaps. Therefore, the existence of the microstructure reduces the resistance of the bionic surface.

## 4. Conclusions

In this work, the microstructure of lotus leaf surface was taken as the research objective. Through numerical simulation and practical experiments, the wettability and drag reduction characteristics of microstructure were studied. The main conclusions are as follows:

(1) The numerical simulation showed that the drag reduction rate of the bionic surface generally increases with the increase of fluid velocity from  $1.0 \text{ m s}^{-1}$  to  $3.0 \text{ m s}^{-1}$ . The drag reduction rate reaches a maximum of 6.29% at a flow velocity of  $3.0 \text{ m s}^{-1}$ . With the increase of velocity, the drag reduction rate begins to decline. The bionic surface begins to lose its drag reduction effect at the flow velocity of  $9.0 \text{ m s}^{-1}$ .

(2) The drag reduction mechanism of the bionic surface is explored. The velocity gradient of the bionic surface is lower than that of smooth surface. The velocity slip occurs on the bionic surface, and the slip length is  $10 \mu\text{m}$ . The contact states between bionic surface and water flow change from Cassie to Wenzel–Cassie state, finally keep in the state of Wenzel with the increase of flow rate.

(3) The static contact angle of the droplet on bionic surface and smooth surface is  $156.6^\circ$  and  $120.4^\circ$ , respectively. The

surface free energy of the bionic surface and smooth surface is  $1.09 \text{ mJ m}^{-2}$  and  $14.26 \text{ mJ m}^{-2}$ , respectively.

(4) In the inclining bench experiment, the water droplets on the smooth surface are hemispherical, but ellipsoidal on the bionic surface, and the center of gravity of water droplet moves forward. The  $\theta_{AB}$  and  $\theta_{RB}$  of water droplet on the bionic surface are  $144.7^\circ$  and  $112.4^\circ$ , and the  $\theta_{AS}$  and  $\theta_{RS}$  of the water droplet on the smooth surface are  $113.1^\circ$  and  $101.2^\circ$ .

This work provides theoretical foundation and new ideas for the drag reduction of underwater vehicles, oil/gas pipelines, etc.

## Author contributions

H. W. and L. W. contributed to the writing of the manuscript, result discussion and the establishment of the model. G. L. and L. C. contributed to the experimental data processing. Y. S. and C. L. contributed to discuss the whole scheme and experimental analysis.

## Conflicts of interest

There are no conflicts to declare.

## Acknowledgements

This study was supported by the National Natural Science Foundation of China (No. 51305282); Key Research Plan of Liaoning, China (No. 2020JH2/10700001).

## References

- 1 W. Barthlott, M. Mail, B. Bhushan and K. Koch, *Nano-Micro Lett.*, 2017, **9**(2), 23.
- 2 Y. Song, Y. Liu, H. Jiang, S. Li, C. Kaya, T. Stegmaier, Z. Han and L. Ren, *Nanoscale*, 2018, **10**(8), 3813–3822.
- 3 R. Jiang, L. Hao, L. Song, L. Tian, Y. Fan, J. Zhao, C. Liu, W. Ming and L. Ren, *Chem. Eng. J.*, 2020, **398**, 125609.
- 4 L. Wang, Q. Gong, S. Zhan, L. Jiang and Y. Zheng, *Adv. Mater.*, 2016, **28**(35), 7729–7735.
- 5 Z. Han, X. Feng, Z. Guo, S. Niu and L. Ren, *Adv. Mater.*, 2018, **30**(13), 1704652.
- 6 Z. Han, Z. Jiao, S. Niu and L. Ren, *Prog. Mater. Sci.*, 2019, **103**, 1–68.
- 7 T. Darmanin and F. Guittard, *Mater. Today*, 2015, **18**(5), 273–285.
- 8 K. Ellinas, P. Dimitrakellis, P. Sarkiris and E. Gogolides, *Processes*, 2021, **9**(4), 66.
- 9 P. Wang, T. Zhao, R. Bian, G. Wang and H. Liu, *ACS Nano*, 2017, **11**(2), 12385–12391.
- 10 P. Hauschwitz, R. Jagdheesh, D. Rostohar, J. Brajer, J. Kopecek, P. Jiricek, J. Houdková and T. Mocek, *Mater. Lett.*, 2019, **256**, 126601.
- 11 Y. Li, H. Mao, P. Hu, M. Hermes, H. Lim, J. Yoon, M. Luhan, Y. Chen and W. Wu, *Adv. Mater. Technol.*, 2019, **4**(5), 1800638.
- 12 A. Das and S. Bhaumik, *J. Micromech. Microeng.*, 2018, **28**(4), 045011.





- 13 B. Bhushan, Y. Jung and K. Koch, *Philos. Trans. R. Soc., A*, 2009, **367**(1894), 1631–1672.
- 14 W. Rong, H. Zhang, Z. Mao, L. Chen and X. Liu, *ACS Omega*, 2022, **7**, 2049–2063.
- 15 B. Bhushan and Y. Jung, *Prog. Mater. Sci.*, 2011, **56**, 1–108.
- 16 R. Daniello, N. Waterhouse and J. Rothstein, *Phys. Fluids*, 2009, **21**(8), 085103.
- 17 X. Sheng and J. Zhang, *Colloids Surf., A*, 2011, **377**, 374–378.
- 18 S. Lyu, D. Nguyen, D. Kim, W. Wang and B. Yoon, *Appl. Surf. Sci.*, 2013, **286**, 206–211.
- 19 Y. Lu, *Surf. Coat. Technol.*, 2017, **331**, 48–56.
- 20 Y. Zhao and X. Huang, *Micromachines*, 2017, **8**(3), 69.
- 21 J. McDonald, D. Duffy, J. Anderson, D. Chiu, H. Wu, O. Schueller and G. Whitesides, *Electrophoresis*, 2000, **20**(1), 27–40.
- 22 E. Shin, S. Lee, G. Kim, J. Jung and C. Lee, *J. Nanosci. Nanotechnol.*, 2020, **20**(11), 6768–6775.
- 23 L. Wu, J. Jiao, Y. Song, W. Ren, S. Niu and Z. Han, *Sci. China: Technol. Sci.*, 2017, **60**(7), 1111–1117.
- 24 L. Tian, Y. Wang, Z. Li, H. Mei and Y. Shang, *Exp. Therm. Fluid Sci.*, 2017, **85**, 363–369.
- 25 P. Ferreira, A. Carvalho, T. Correia, B. Antunes, I. Correia and P. Alves, *Sci. Technol. Adv. Mater.*, 2013, **14**(5), 055006.
- 26 L. Wu, H. Wang, Y. Song, B. Zhang, Y. Xu, C. Liu and Y. Yan, *Sci. Rep.*, 2020, **10**, 12873.
- 27 L. Tian, Y. Wang, Z. Li and Y. Shang, *Appl. Therm. Eng.*, 2017, **123**, 1152–1157.
- 28 C. Teo and B. Khoo, *Microfluid. Nanofluid.*, 2010, **9**(2–3), 499–511.
- 29 K. Li, X. Zeng, H. Li, X. Lai, C. Ye and H. Xie, *Appl. Surf. Sci.*, 2013, **279**, 458–463.
- 30 D. Kwok and A. Neumann, *Adv. Colloid Interface Sci.*, 1999, **81**(3), 167–249.
- 31 J. Chen, J. Chen, L. Li, S. Wang and Y. Xie, *Eur. Phys. J. E.*, 2021, **44**(2), 25.

